

Local Maximum Likelihood Segmentation of Echocardiographic Images with Rayleigh Distribution

Ahror Belaid · Djamel Boukerroui

Received: 25 July 2017 / Revised: 26 December 2017 / Accepted: 28 January 2018

Abstract In order to interpret ultrasound images, it is important to understand their formation and the properties that affect them, especially speckle noise. This image texture, or speckle, is a correlated and multiplicative noise that inherently occurs in all types of coherent imaging systems. Indeed, its statistics depend on the density and on the type of scatterers in the tissues. This paper presents a new method for echocardiographic images segmentation in a variational level set framework. A partial differential equation-based flow is designed locally in order to achieve a maximum likelihood segmentation of the region of interest. A Rayleigh probability distribution is considered to model the local B-mode ultrasound images intensities. In order to confront more the speckle noise and local changes of intensity, the proposed local region term is combined with a local phase-based geodesic active contours term. Comparison results on natural and simulated images show that the proposed model is robust to attenuations and captures well the low contrast boundaries.

Keywords Echocardiography · Level set segmentation · Local phase · Monogenic signal · Maximum likelihood

1 Introduction

Ultrasound imaging represents one of the most popular exploration techniques commonly used in many diagnostic and therapeutic applications. It has many advantages: it is non-invasive, provides images in real time and requires lightweight material. However, ultrasound images segmentation is particularly difficult mainly due to the low signal-to-noise ratio, low contrast and high amounts of speckle. This image texture, or speckle, is a correlated and multiplicative noise that inherently occurs in all types of coherent imaging systems. Hence, it makes modeling difficult as its statistics depend on the density and the

A. Belaid
Medical Computing Laboratory (LIMED), University of Abderrahmane Mira, 06000, Bejaia, Algeria, E-mail: ahror.belaid@univ-bejaia.dz

D. Boukerroui
Mirada Medical Ltd, New Road, Oxford OX1 1BY, UK, E-mail: djamal.boukerroui@mirada-medical.com.
Sorbonne universits, Universit de Technologie de Compigne, CNRS 7253 UMR/Heudiasyc. CS 60319, 60203 Compigne cedex.

type of scatterers in the tissues (see e.g., [46]). All these characteristics make segmentation difficult and therefore complicate the diagnosis task [48].

Our study in this work is restricted to echocardiographic data. It is known that echocardiography has been one of the driving application areas of medical ultrasound and the literature on methods for automatically segmenting and tracking the left ventricle is extensive. As it has been pointed out in [48], the most popular approach designed to treat echocardiographic endocardial segmentation is a contour finding approach. This is not straightforward as the contrast around the left ventricle chamber boundaries varies, depending on its relative orientation to the transducer direction and to attenuations.

This paper concerns the development of a novel region-based active contour model in a variational level-set framework. First, we use a kernel function to define a local energy around a given point. This energy characterizes the fitting of the local Rayleigh distribution to the local image data around a neighborhood of a point. This local energy is then embedded over the entire image domain. The local intensity *pdf* parameter, which is spatially a varying function, is a variable of the energy functional and is estimated locally using the Maximum Likelihood principle. The minimization of the energy functional is achieved by solving the gradient-descent flow equation. The final evolution equation is then simplified to an easy equation to handle.

The work presented in this paper is a study of the adaptation of the global model proposed by Sarti et al. [54]. Our method is hybrid, it combines a local region-based term and a contour-based term derived from the GAC (Geodesic Active Contours). The latter uses local phase information derived from the *monogenic signal* [30,31] to detect edges. Some preliminary results of this study have been presented in [6]. Here the images database is expanded to 50 new manual delineations corresponding to 5 new B-mode images. Moreover, a new database including 60 synthetic (B-mod and RF) images is carried out. The quadrature filter used for the edge detection term is the α scale spaces derivative (ASSD) filter instead of Cauchy filter. We chose to use this filter because it has been proven that this filter responds well on ultrasound images as shown in [8].

B-mode ultrasound images segmentation methods (overall, focused on the echocardiographic images) are reviewed in the next section. After that, Section 3 introduces a brief description about the monogenic edge detection measure, called *Monogenic Feature Asymmetry*. The proposed segmentation method is presented in Section 4. Section 5 shows preliminary experimental results on real and synthetic data. Section 6 provides a discussion followed by some concluding remarks.

2 Background

Several ways to classify ultrasound segmentation methods, can be found in the literature. One of the most popular way is the classification according to their level of complexity (low, intermediate and high level). There are other frequently encountered types of classification based on whether the approaches are global, contours, region or continuous. In this paper, we opted for characterizing methods in terms of a priori knowledge or constraints used to resolve the segmentation problem. This new view of methods classification is inspired by that presented in [47]. Based on this formalism, two types of constraints are distinguished. Firstly, the constraints related to the information that can be extracted from the image or imaging system; secondly, the constraints related to the nature of the object concerned by segmentation, as its anatomy or its physiological behavior.

2.1 Constraints related to the image and imaging

2.1.1 Gray level distribution

Backscattering energy of echo signals create interference patterns in the acquired signal called speckles. These inherent speckles degrade the resolution of the signal and corrupt the specificity of gray level intensities. Several empirical models were used to describe the gray level distribution. As known in the literature, fully developed speckle noise in envelope-detected ultrasound signals can be modeled by Rayleigh distribution. Indeed, the Rayleigh model is the most commonly used to describe the speckle phenomenon [11, 18, 35, 54, 48, 5, 3, 56, 25, 13, 1]. This model is embedded in the more general Rician noise model that also applies to MRI noise [53, 63]. In case of low SNR, as in ultrasound, the Rician distribution tends to a Rayleigh distribution, while at high SNR, as in high quality MRI, the Rician distribution tends to a Gaussian distribution [58, 64]. In order to account for the non-Rayleigh scattering, a number of distributions have been proposed, including the K-distribution [28], the Nakagami distribution [55], the Weibull distribution [32], and Generalized Gamma (GG) distribution [52].

The Rayleigh model has been used for edge detection by anisotropic diffusion [57], and in the methods of statistical segmentation [42, 18, 35]. Good results of segmentation on the B-mode images have also been obtained by Slabaugh et al. [56] and Sarti et al. [54] incorporating the Rayleigh distribution in the level sets method. Other similar results in [3, 6] have been obtained using the same principle. One can find other distributions models also used in segmentation algorithms, for example, we can mention the Gaussian [11], exponential [50], Gamma [60], Beta [41] and Rician Inverse Gaussian distributions [29].

Certainly, the gray level distribution allows the characterization of different tissues, but unfortunately this modelization does not take into account some spatial effects such as attenuation, acoustic shading and the signal dropout. To overcome these drawbacks, some authors reinforce their models by adding other constraints as the information about contours [40, 62, 6]. Furthermore, to address the attenuation problem, other authors propose to model the gray level distribution on a limited local area, and not globally [11, 4, 38, 17, 64, 6, 15, 65]. More details on this methods will be presented subsequently.

2.1.2 Differential operators

The derivative of the intensity has proven to be a widely used method in many image processing areas for detecting the change in intensity as contours. Indeed, the maximum of the first derivative (or the zero crossing of the second derivative) can locate the change of intensity and discontinuities in the form of a *step edge*. These intensity changes and discontinuities are generally associated with the contours of objects in the image [21, 40, 41]. In the case of ultrasound images, this method is only efficient in the presence of strong acoustic discontinuities between different tissues. In addition, because of the anisotropic acquisition of ultrasound images, some object boundaries are often not detected or not at all. Although very good progress has been made in the area of edge detection, gradient empirical estimation techniques proposed in the 80s are often still used in competition with more modern techniques. Indeed, the gradient operator used for edge detection is formal, but unfortunately sterile.

2.1.3 Phase information

Some authors have shown that to detect the acoustic surfaces, the local phase information of the image is more robust than the intensity gradient [43, 37, 45, 66, 7, 65]. By measuring the local phase or the *phase congruency* at several scales, this allows to characterize the intensities differences in term of *shape* and not in term of *strength* of intensity. Indeed, the signal amplitude (or gradient) informs us about the strength of discontinuities, while the local phase provides information of the shape, making it independent to changes of intensity. Morrone and Burr [43] have shown that the visual perception structures (structures that the human eye identifies as interesting) is associated with positions where the phases are in congruence, i.e. the points where the Fourier components are in phase. Thus, there is a strong link between the phase congruence and the presence of relevant characteristics. These points also inform us about the type of the detected structure, including lines and edges. For example, 0 or π as values of the local phase, correspond to a stair type discontinuity.

2.1.4 Texture measures

Because of the granular appearance of ultrasound image, texture is considered as a useful feature for classification or regions based segmentation methods [11, 27, 49]. These methods have had some limited success in the scientific community. The image texture is dependent on the microstructure of the tissue and the imaging system used. Different systems lead to different patterns of texture, and therefore these methods do not reflect the true characterization of the physical properties of the tissue. Moreover, the characterization of image texture is highly dependent on the spatial scale of analysis and requires the use of a multi-resolution approach [47].

2.2 Constraints relating to the structure of interest

2.2.1 Anatomy - shape -

Often, region information (homogeneity constraint) and contour (discontinuity) are not enough to achieve a reliable and accurate segmentation. In the case of dropout ultrasound signal, the region and contour information cannot identify the region of interest. Shape constraint is often a successful solution to improve the segmentation results. The shape model, also called *deformable model* or active shape model is a segmentation technique originally introduced by Cootes et al. [23] to locate deformable objects in images. It is mainly based on a priori knowledge of the shape and deformation modes of the structure of interest. The shape constraint may be embedded into the segmentation model by different ways. For example, using in particular an explicit form of representation as the point distribution model [23]. The first applications of such formalism to active contours, have proven ineffective for treating complex shapes. Non-parametric approaches, better suited to general medical applications, are developed. The formalism of the level sets can implement these methods effectively and topological changes are permitted [67, 26]. Thanks to their robustness to attenuations, shading artifacts and speckle, ultrasonic B-mode images segmentation methods based on shape constraints have been widely used in recent years. A more complete view can be found in [48, 24, 33].

2.2.2 Physiology - motion -

One of the reasons of the frequently use of ultrasound imaging is that it provides dynamic images. Therefore, the literature on the spatio-temporal segmentation is very broad. The typical example that we can mention is the segmentation of cardiac images, the structure has a quasi-periodic motion. Several applications and motion-based models can be readily found in the literature. One can in particular refer to the survey of Noble et Boukerroui in [48].

The motion constraint can be injected into the segmentation model following several assumptions: for example, assuming a local or global temporal coherence [21,2], assuming a constant velocity [34], or including time explicitly in the optimization process as in [10]. Zhu et al. [67] have introduced a new constraint to the movement that is the incompressibility of myocardium. The authors assume that during the cardiac cycle the myocardium is almost incompressible and its volume undergoes changes that are less than 5%. Recently, Porras et al. [51] have proposed a technique for myocardial motion estimation based on image registration using both B-mode echocardiographic images and tissue Doppler sequences. Finally, this constraint list is not comprehensive, many other constraints such as similarity measures can be found in the literature [48].

3 Method

3.1 Monogenic signal

One of the popular methods to estimate local signal information (amplitude, phase and orientation) is based on the analytic representation of this signal. Felsberg and Sommer [30, 31], have proposed a novel n-dimensional generalization of the analytic signal. In particular, they proposed a 2D isotropic analytic signal, called *monogenic signal*.

For a given 2D signal $f(\mathbf{x})$, the monogenic signal can be represented by a scalar-valued even and vector-valued odd filtered responses, with the following simple tick:

$$\begin{aligned} \text{even} &= c * f \text{ ,} \\ \text{odd} &= (c * h_1 * f, c * h_2 * f) \text{ ,} \end{aligned}$$

where c is the spatial domain representation of an isotropic bandpass filter, and $\mathbf{h} = (h_1, h_2)$ is the generalized Hilbert transform kernel,

$$\mathbf{h}(\mathbf{x}) = (h_1, h_2) = \frac{1}{2\pi} \frac{\mathbf{x}}{\|\mathbf{x}\|^3} \text{ .}$$

Recently, Belaid et Boukerroui in [9] have introduced a new quadrature filter kernel called α scale spaces derivative filters (ASSD). We chose to use this filter because it seems to be efficient on ultrasound images as shown in [8]. In the frequency domain, a 2D isotropic ASSD kernel is defined by:

$$\mathcal{C}_{ASSD}(\mathbf{u}) = \begin{cases} n_c \mathbf{u}^a \exp(-(s\mathbf{u})^{2\alpha}) & \text{if } \mathbf{u} \geq 0 \text{ ,} \\ 0 & \text{otherwise ,} \end{cases} \quad (1)$$

where $\mathbf{u} = (u_1, u_2)$, s is a scaling parameter and $a \in \mathbb{R}^+$ is the fractional order derivatives of the filter. Typical values of α are in the range [0.51]. n_c is a normalization constant.

3.2 Monogenic Feature Asymmetry

Step edge detection is performed using the *feature asymmetry* measure (FA) of Kovesi [37] defined, in this paper, using the previously presented monogenic signal. The identification of step edges essentially involves finding points where the absolute value of the local phase is 0° at a positive edge and 180° at a negative edge. In other words, the difference between the odd and the even filter responses is large. Kovesi suggested to use FA over a number of scales to detect step edge features. We define the multiple scales monogenic feature asymmetry:

$$FA_{MS} = \frac{1}{N} \sum_s \frac{[|\mathbf{odd}_s| - |\mathbf{even}_s| - T_s]}{\sqrt{\mathbf{even}_s^2 + \mathbf{odd}_s^2 + \varepsilon}}, \quad (2)$$

where N is the total number of scales, $[\cdot]$ denotes zeroing of negative values and T_s is the scale specific noise threshold [37]. For a given scale, the FA takes values in $[0, 1]$, close to zero in smooth regions and close to one near boundaries.

The application of Kovesi's FA in [44] on ultrasound images has yielded good results. The authors used steerable filters for the 2D extension. The authors in [7] used the monogenic signal, as it is the natural extension of the 1D analytical signal. The monogenic feature asymmetry applied on ultrasound images yielded better results.

4 Segmentation model

Let I denote a given image defined on the domain Ω , and let \mathcal{C} be a closed contour represented as the zero level set of a signed distance function ϕ , i.e., $\mathcal{C} = \{\mathbf{x} | \phi(\mathbf{x}) = 0, \mathbf{x} \in \Omega\}$. We specify the interior of \mathcal{C} by a smooth approximation of the Heaviside function $H(\phi)$. Similarly, the exterior of \mathcal{C} is defined as $(1 - H(\phi))$.

We introduce the following classical energy functional to be minimized [19, 54]:

$$\begin{aligned} E_G(\phi) &= \mathcal{L}_G(\phi) + \mathcal{R}_G(\phi) \\ &= \lambda \int_{\Omega} g\delta(\phi)|\nabla\phi|d\mathbf{x} \\ &\quad - \int_{\Omega} H(\phi) \log p(I, \sigma_i) d\mathbf{x} - \int_{\Omega} (1 - H(\phi)) \log p(I, \sigma_o) d\mathbf{x} . \end{aligned} \quad (3)$$

This energy model is composed of two terms: a gradient edge-based term $\mathcal{L}_G(\phi)$ and a global region-based term $\mathcal{R}_G(\phi)$. The first is the Geodesic Active Contour term (GAC) [20], where λ is a positive fixed parameter and g is an inverse edge indicator function, generally taken as $g(x, y) = 1/(1 + |\nabla G_s * I|)$. Here, G_s is the Gaussian kernel with standard deviation s . The second is a global region-based term. Specifically, it is the log likelihood function to maximize, given by the product of the inner and the outer probabilities [16, 19]. Here, $p(I, \sigma)$ represents the probability density function characterizing the observed gray level of image I . σ_i and σ_o represent the parameters of the *pdf* respectively inside and outside the curve.

In the following, we define an alternative energy function, similar to the form of (3), but using local image properties. We use a local phase-based edge indicator function $g = 1 - FA_{MS}^\gamma$ instead of the classical inverse gradient-based one. Here, γ is a scale parameter and $FA_{MS} \in [0, 1]$ represents the monogenic feature asymmetry measure defined by (2). This allows us to define the local phase-based GAC term noted $\mathcal{L}_p(\phi)$. As it was mentioned in the

introduction, recent works showed that ultrasound images respond well to phase-based edge detection. Moreover, a multi-scales approach offers a better control on the edge detection quality.

Now, we focus on our new local region term. Classical region-based methods, like the ML model, often make strong assumptions on the intensity distributions of the searched object and background. In order to be less restrictive, the local energy achieves a trade off between the local features and the global region. Localizing the region term seems to be a good alternative to avoid the attenuation artifact, which is one of the main characteristics of ultrasound images. We aim in the remainder of this section to change this term \mathcal{R}_G to a new local region-based term \mathcal{R}_L [39,38,17]. This term is a local version of the one presented by Sarti et al. in [54].

Precisely, the proposed model is derived from [38]. The proposed model in [39,64] is considered as a special case of the one presented in [38]. Values of level set function are estimated only in a narrow band around the zero level set, which is not the case in [39,64]. The functional of our model is an adaptation of that presented in [38]. The local intensity *pdf* parameter is estimated locally using the Maximum Likelihood principle. The minimization of the energy functional is achieved by solving the gradient-descent flow equation. The final evolution equation is then simplified to an easy equation to handle.

In the work of Brox and Cremers [17], the authors assume that pixel intensities are realizations of the random (Gaussian) variable and are not, as usual, identically distributed but the distribution varies with the position in the image. As we have already mentioned previously, the most commonly used statistical intensity model for ultrasound images is the Rayleigh distribution $p(I) = I/\sigma^2 \exp(-I^2/2\sigma^2)$. Thus, here we also assume that observed intensities are independent Rayleigh random variables. We also assume, as in [17], that the identically distributed assumption is valid only locally.

To achieve this, we introduce the following characteristic function \mathcal{B} used to define a local region in terms of a radius parameter r [38],

$$\mathcal{B}(\mathbf{y}; \mathbf{x}) = \begin{cases} 1, & \|\mathbf{x} - \mathbf{y}\| < r \\ 0, & \text{otherwise} . \end{cases}$$

Thus, the local region version around a given point \mathbf{x} , of the global region term \mathcal{R}_G in (3), is given by:

$$F(\phi; \mathbf{x}) = - \int_{\Omega} \mathcal{B}(\mathbf{y}; \mathbf{x}) H(\phi(\mathbf{y})) \log p(I(\mathbf{y}), \hat{\sigma}_i(\mathbf{x})) d\mathbf{y} \quad (4)$$

$$- \int_{\Omega} \mathcal{B}(\mathbf{y}; \mathbf{x}) (1 - H(\phi(\mathbf{y}))) \log p(I(\mathbf{y}), \hat{\sigma}_o(\mathbf{x})) d\mathbf{y} .$$

This formulation allows us to estimate the *pdf* parameter σ^2 locally, inside and outside the curve. The local ML estimates are given by:

$$\hat{\sigma}_i^2(\mathbf{x}) = \frac{1}{2M_i(\mathbf{x})} \int_{\Omega} \mathcal{B}(\mathbf{y}; \mathbf{x}) H(\phi) I(\mathbf{y})^2 d\mathbf{y} ,$$

$$\hat{\sigma}_o^2(\mathbf{x}) = \frac{1}{2M_o(\mathbf{x})} \int_{\Omega} \mathcal{B}(\mathbf{y}; \mathbf{x}) (1 - H(\phi)) I(\mathbf{y})^2 d\mathbf{y} ,$$

where M_i and M_o denote respectively the local area inside and outside Ω and are given as:

$$M_i(\mathbf{x}) = \int_{\Omega} \mathcal{B}(\mathbf{y}; \mathbf{x}) H(\phi) d\mathbf{y} ,$$

$$M_o(\mathbf{x}) = \int_{\Omega} \mathcal{B}(\mathbf{y}; \mathbf{x}) (1 - H(\phi)) d\mathbf{y} .$$

By introducing these estimates back in the local log likelihood (4), we obtain the new formulation:

$$F(\phi; \mathbf{x}) = -M_i(\mathbf{x}) \log \left(\frac{1}{M_i(\mathbf{x})} \int_{\Omega} \mathcal{B}(\mathbf{y}; \mathbf{x}) H(\phi(\mathbf{y})) I(\mathbf{y})^2 d\mathbf{y} \right) \\ - M_o(\mathbf{x}) \log \left(\frac{1}{M_o(\mathbf{x})} \int_{\Omega} \mathcal{B}(\mathbf{y}; \mathbf{x}) (1 - H(\phi(\mathbf{y}))) I(\mathbf{y})^2 d\mathbf{y} \right) .$$

By bringing the local phase and local region terms, we now define our new energy built from (3) as follows:

$$E_L(\phi) = \mathcal{L}_P(\phi) + \mathcal{R}_L(\phi) \quad (5) \\ = \lambda \int_{\Omega} g \delta(\phi) |\nabla \phi| d\mathbf{y} + \int_{\Omega} \delta(\phi(\mathbf{x})) F(\phi; \mathbf{x}) d\mathbf{x} ,$$

$F(\cdot; \mathbf{x})$ represents a local image contribution at each point along the curve evolution.

This formulation is under the assumption that the local behavior of an ultrasound image follows the Rayleigh distribution, and assuming that the size of this local region is sufficient for a maximum likelihood estimation of the parameter σ .

It is straightforward to see that the mask $\mathcal{B}(\mathbf{y}; \mathbf{x})$ is independent of ϕ . Thus, the associated flow equation of $F(\phi; \mathbf{x})$ is given by:

$$F_{LML}(\phi; \mathbf{z}; \mathbf{x}) = \log \left(\frac{1}{M_i(\mathbf{x})} \int_{\Omega} \mathcal{B}(\mathbf{y}; \mathbf{x}) H(\phi(\mathbf{y})) I(\mathbf{y})^2 d\mathbf{y} \right) \quad (6) \\ + \frac{I(\mathbf{z})^2 M_i(\mathbf{x}) + \int_{\Omega} \mathcal{B}(\mathbf{y}; \mathbf{x}) H(\phi(\mathbf{x})) I(\mathbf{y})^2 d\mathbf{y}}{\int_{\Omega} \mathcal{B}(\mathbf{y}; \mathbf{x}) H(\phi(\mathbf{x})) I(\mathbf{y})^2 d\mathbf{y}} \\ - \log \left(\frac{1}{M_o(\mathbf{x})} \int_{\Omega} \mathcal{B}(\mathbf{y}; \mathbf{x}) (1 - H(\phi(\mathbf{y}))) I(\mathbf{y})^2 d\mathbf{y} \right) \\ + \frac{I(\mathbf{z})^2 M_o(\mathbf{x}) + \int_{\Omega} \mathcal{B}(\mathbf{y}; \mathbf{x}) (1 - H(\phi(\mathbf{y}))) I(\mathbf{y})^2 d\mathbf{y}}{\int_{\Omega} \mathcal{B}(\mathbf{y}; \mathbf{x}) (1 - H(\phi(\mathbf{y}))) I(\mathbf{y})^2 d\mathbf{y}} ,$$

in agreement with [54].

Finally, the gradient descent flow minimizing (5), in the level set formulation, is given by (see Appendix):

$$\frac{\partial \phi}{\partial \tau}(\mathbf{x}) = \delta(\phi(\mathbf{x})) \left[\lambda \operatorname{div} \left(g(\mathbf{x}) \frac{\nabla \phi(\mathbf{x})}{|\nabla \phi(\mathbf{x})|} \right) \quad (7) \right. \\ \left. + \int_{\Omega} \delta(\phi(\mathbf{y})) \mathcal{B}(\mathbf{y}; \mathbf{x}) F_{LML}(\phi; \mathbf{y}; \mathbf{x}) d\mathbf{y} \right] .$$

5 Results

In order to evaluate the proposed method and quantify its accuracy, we have compared the results of our proposed approach with those of other closely related algorithms. The variational proposed approach was applied to a variety of natural and synthetic images.

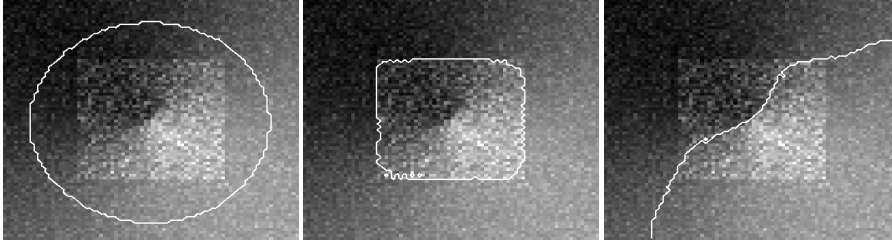


Fig. 1 Comparison of the local and global ML model. Left to right: Initial contour and original synthetic image, segmentation using respectively local and global ML region term only.

Three quantitative measures have been used. An area overlap ratio, namely the Dice Similarity Coefficient (DSC)

$$DSC(S, S_{ideal}) = 2 \frac{|S \cap S_{ideal}|}{|S| + |S_{ideal}|} ,$$

and two metric distances: the Mean Absolute Distance (MAD) which measures an average error and the Hausdorff Distance (HD) accounting for maximum errors between two contours. The Mean Absolute Distance is given by [59]:

$$MAD(\mathcal{C}_1, \mathcal{C}_2) = \frac{1}{2} \left[\frac{1}{n} \sum_{i=1}^n d(a_i, \mathcal{C}_2) + \frac{1}{m} \sum_{i=1}^m d(b_i, \mathcal{C}_1) \right] ,$$

where, $\mathcal{C}_1 = \{a_1, a_2, \dots, a_n\}$, $\mathcal{C}_2 = \{b_1, b_2, \dots, b_m\}$ are the curves represented by an ordered set of coordinate pair of points and $d(a_i, \mathcal{C}_2) = \min_{b_j \in \mathcal{C}_2} \|b_j - a_i\|$ represents the euclidian distance between the point a_i and the nearest point in the curve \mathcal{C}_2 . The Hausdorff Distance is given by:

$$HD(\mathcal{C}_1, \mathcal{C}_2) = \max \left\{ \sup_i d(a_i, \mathcal{C}_2), \sup_i d(b_i, \mathcal{C}_1) \right\} .$$

The closer the DSC and the MAD (also HD) values to 1 and 0 respectively, the better is the segmentation.

In all of the experimental results, the radius of the localizing ball r was fixed to 11 pixels. Unless otherwise stated, the regularization term parameter λ is set to 0.6. The following ASSD filter parameters were fixed as such: bandwidth $\in \{2.5, 1.5\}$ octaves as suggested in [12], wavelength is 23 pixels for real images and is 7 and 9 pixels respectively for B-scan and RF simulated images.

A comparison between the global and local models is highlighted by a simple experiment that illustrates the influence of attenuation in the segmentation process. We built for this purpose a test image which reproduces some properties of ultrasound images. Fig.1 demonstrates the effect of a non-uniform illumination with speckle noise and contains a shape of a low-contrast square structure. The edge-based term is turned off, while the region term plays the leading role. In this case, the local region-based term gives a successful result while the global region-based segmentation algorithm fails, and partitions the image into two regions of different attenuations.

5.1 Evaluation with manual segmentations

As a preliminary validation, we have compared the semi-automatic algorithm results to manual segmentations. We have collected a set of 15 bidimensional cardiac ultrasound images for different patients, obtained from a Philips IE33 echocardiographic imaging system. The data set was segmented by two specialists in an independent way, i.e. in different days. Each specialist segments each image 5 times, in order that 10 manual segmentations are available for each image. Thus, in all, we have 150 manual segmentations. This allows measuring the inter and intra-observer variabilities, that are the difference delineations performed by the same specialist as well as the difference between segmentations performed by different specialists, respectively.

The comparison between the computer versus the manually traced contours resulted in a perfect agreement in the areas calculated with both techniques, with a very good correlation ($r = 1$). In Fig. 2 the linear regression and Bland-Altman results are graphically reported. An example of the automated versus the manually traced contours is shown in Fig. 3 (right) where the good correspondence can be appreciated. In the same figure, we can see an illustrative comparison results of the proposed segmentation algorithm and the results of the global ML algorithm [54] with manual delineation. These results give the reader some insight regarding the robustness to speckle noise and to attenuation. Note that, the manual segmentation seems to be more regular than the automatic one.

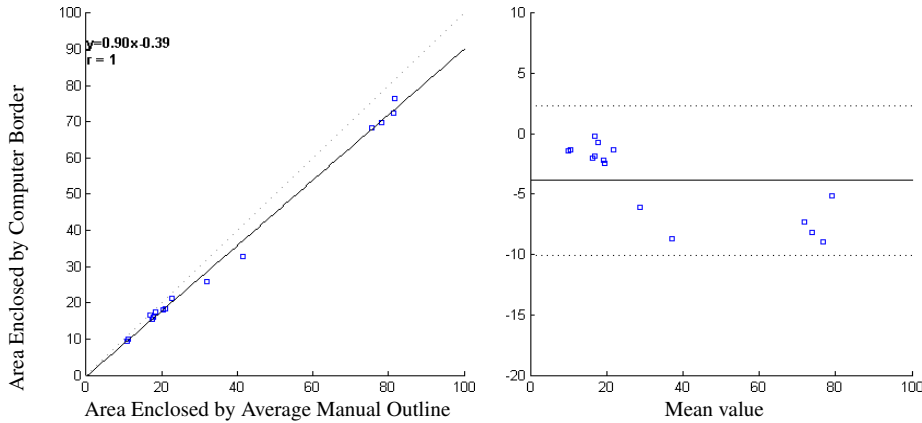


Fig. 2 Linear regression analysis (left) and Bland-Altman analysis (right) comparing average manual tracing and area values obtained applying our local maximum likelihood segmentation method. The areas are in mm^2 . The dashed line is the unity line.

The experiment in Fig. 4 shows the performance of the monogenic feature asymmetry to detect step edge boundaries in very noisy and low contrast data. The adverse effect of FA measure is the delocalization, by moving closer to finer scales, the FA measure recovers details and discontinuities, but loses the regularity and the continuity of the boundaries. This drawback can be reduced by using a multiscale detection, see Equation (2). Are shown in the same figure, illustrative results of our method on two typical ultrasound images (left ventricle).

Table 1 and 2 show a quantitative comparison between our approach -noted LP+LML for Local Phase with a Local ML model- and two semi-automatic segmentation methods:

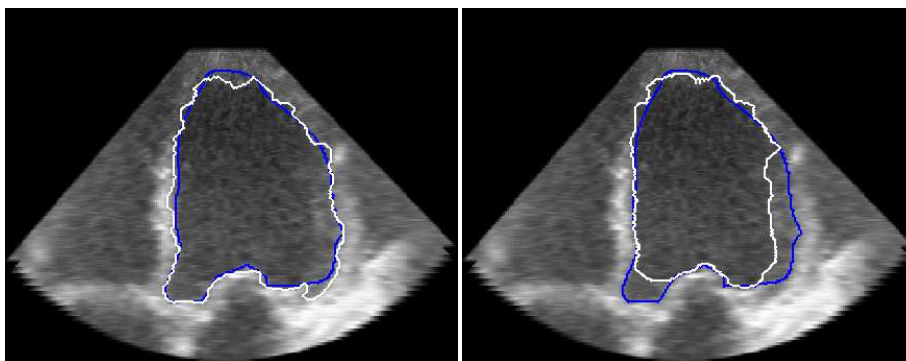


Fig. 3 Comparison of the proposed method (left) and the global ML model (right) with a manual delineation. Blue line: manual delineation, white line: semi automatic segmentation. Parameter $\lambda = 0.7$.

Table 1 Performance indices measures DSC, MAD and HD versus Interobserver, Intraobserver and computer-observer distances. The mean, median and standard deviation for DSC, MAD and HD are shown. The comparison is performed here between the computer results and all the manual segmentations.

Measures	DSC (%)			MAD (pixels)			HD (pixels)		
	Mean	Median	SD	Mean	Median	SD	Mean	Median	SD
GAC	88.25	89	4.82	5.81	5.06	1.85	17.6	15.16	7.95
GAC+GML	90.22	91.10	3.96	4.8	4.67	1.61	18.38	18.98	6.70
LP+LML	91.62	91.93	2.24	4.69	3.49	2.1	14.44	12.64	5.33
Interobserver	94.73	96.40	3.19	2.94	3.02	1.16	8.91	8.46	3.52
Intraobserver	96.32	96.54	0.79	2.25	2.11	0.65	7.95	7.29	2.62

Table 2 Performance indices measures DSC, MAD and HD versus Interobserver, Intraobserver and computer-observer distances. The mean, median and standard deviation for DSC, MAD and HD are shown. The comparison is performed here between the computer results and the mean of the manual segmentations.

Measures	DSC (%)			MAD (pixels)			HD (pixels)		
	Mean	Median	SD	Mean	Median	SD	Mean	Median	SD
GAC	88.78	89.57	4.94	5.54	4.83	1.87	16.69	15.04	8.23
GAC+GML	90.79	91.45	4.01	4.53	4.33	1.59	17.87	18.14	7.02
LP+LML	92.30	93.2	2.34	4.4	3.23	2.09	13	11.67	5.36
Interobserver	94.73	96.40	3.19	2.94	3.02	1.16	8.91	8.46	3.52
Intraobserver	96.32	96.54	0.79	2.25	2.11	0.65	7.95	7.29	2.62

classical GAC and GAC with a global ML model (GAC+GML). Inter and Intra-observer values are also shown in this table. The mean, median and standard deviation of all the echocardiographic images segmentations are shown for the three measures: Dice similarity coefficient, mean absolute distance and Hausdorff distance (See, for example, [22,67,7]). Table 1 reports the results of the distance between the algorithm and all the manual delineations, while Table 2 reports the results of the distance between the algorithm and the mean manual delineations of each physician. As expected, comparison results with the average manual segmentation are better than those compared with all manual segmentations, the error and the standard deviation decrease. It can be noted that, the intraobserver values are lower than those of the inter-observer, and much less than those of all the automatic methods (GAC, GAC+GML and LP+LML). The low standard deviations of the intraobserver let us assume regular segmentations of the two specialists.

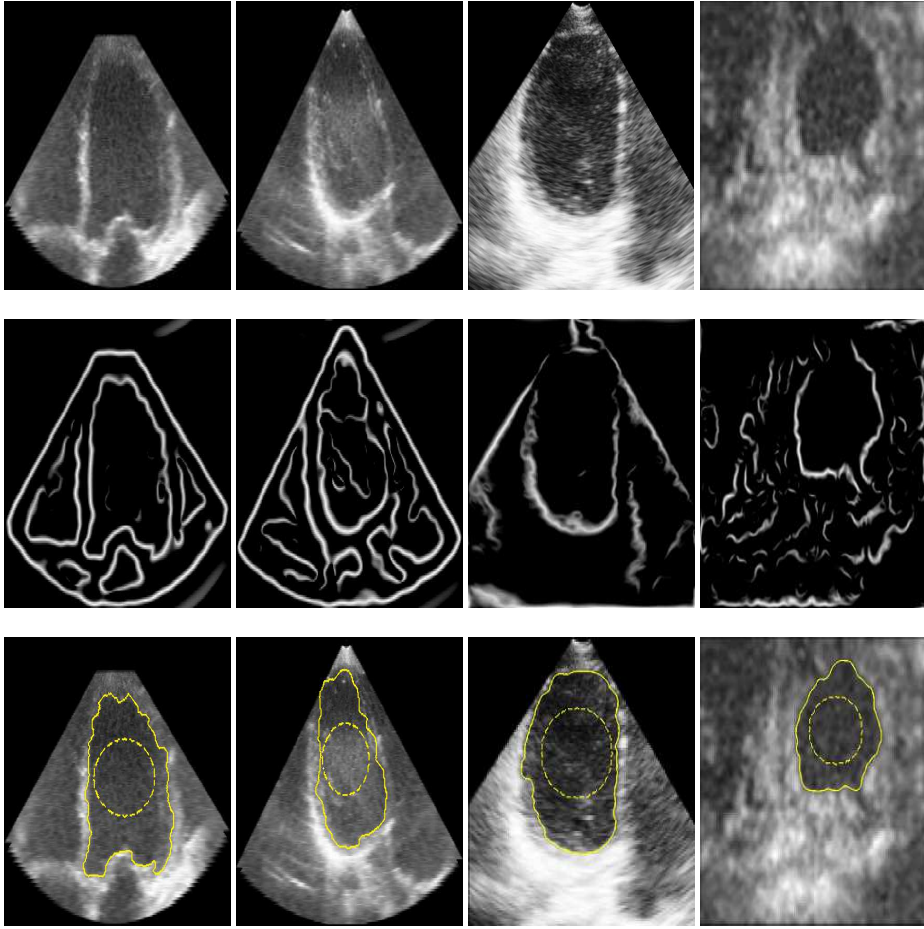


Fig. 4 Examples of the proposed model segmentation results in echocardiographic images. Top of the figure: the original images, in the middle: the edge detections performed by the monogenic feature asymmetry. Bottom: segmentation results. The inner dashed contours are the respective initializations. In this experiments, $\lambda = 0.7$.

5.2 Evaluation on simulated ultrasound images

In order to demonstrate the usefulness of the proposed approach, we chose, among others, to test it on realistic US simulations. To this end, we have used the simulated ultrasound images with ground truth contours by Boukerroui [13]. He used the simulation program Filed-II [36], to synthesize phantom data with known ground truth. A linear scan of a first phantom (PH1) was done with a 290 elements transducer using 64 active elements. The scatterers in the phantom were randomly distributed within the phantom of $80 \times 80 \times 15$ mm cube size. 128 lines were simulated at 5 Mhz. The second phantom (PH2) of size $100 \times 100 \times 15$ mm cube was placed at 10 mm depth from the transducer surface, and was scanned with a 7 MHz 128 elements phased array transducer. The images consist of 128 lines with 0.7 degrees between lines. Hanning apodization in transmitting and receiving was

Table 3 Performance indices measures DSC, MAD and HD versus LGDF and LP+LML models, on simulated images. The mean, median and standard deviation for DSC, MAD and HD are shown.

Measures	DSC (%)			MAD (pixels)			HD (pixels)		
	Mean	Median	SD	Mean	Median	SD	Mean	Median	SD
LGDF [64]	92.31	93.70	5.04	3.53	1.33	3.59	7.87	3.4	7.41
LP+LML	95.33	95.7	1.04	1.39	1.04	1.43	3.92	3.21	2.82

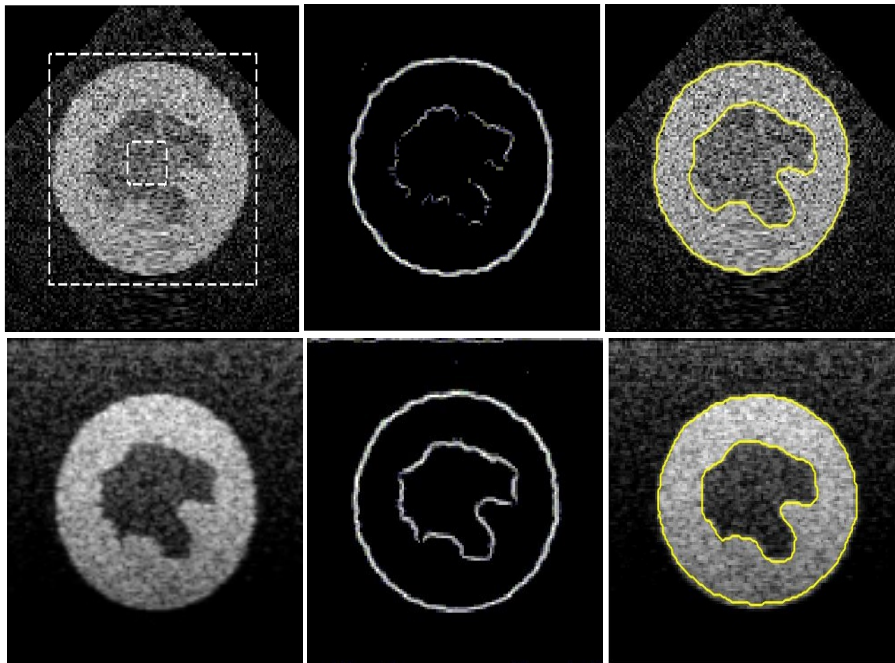


Fig. 5 Illustrative segmentation results of the local Rayleigh model on simulated B-mode (Top) and RF (bottom) images. From right to left: original image, FA edge detection and final result. Dashed line on the top right image shows the initialization.

used in all experiments. Two scatterers amplitudes with three levels of tissue attenuations were simulated for both phantoms. We also used several dB ranges for the envelope logarithmic compression to simulate different image contrasts [13]. Some typical images are shown in Fig. 5 and 6.

In sum, our proposed method was evaluated on 60 realistic simulated ultrasound images with known ground truth. Table 3 summarizes the results of the comparison of our approach, and the model called *Local Gaussian Distribution Fitting* (LGDF) presented in [64].

Experiments on simulated data also confirm our observations about the performance of the proposed method. The results obtained by the LP+LML method are better than those of the LGDF model; although, the LGDF model also provides acceptable results, as we can see in Table 3. Segmentation by LP+LML provides the best results in terms of average performance and in terms of regularity, and also in terms of standard deviation. The LGDF model does not fail also in terms of average performance. We have not shown the results obtained by the global methods because in most cases the curves of the level set fail.

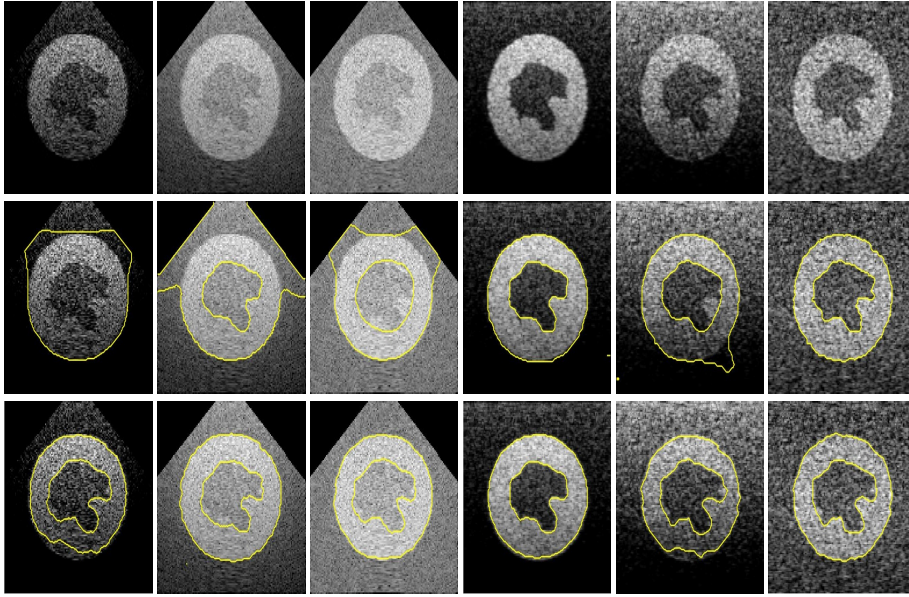


Fig. 6 Illustrative segmentation results of the local Rayleigh model on simulated US images with different: tissues characteristics, attenuation level and log compression parameters. From top to bottom: Original images, LGDF model results and proposed approach results.

The performance of the proposed approach compared to the LGDF model can be justified by firstly the edge-based term added to reinforce the detection. Secondly, our energy function is more localized than the LGDF model. Indeed, the two integrals of the local term are multiplied by the Dirac function in order to make the calculation only around the neighborhood of the contour and not on the whole image, see Equation (5); while we can see, in [64] Equation (13), that the integral of the LGDF local term makes calculation on the whole image.

6 Discussion

The quantitative evaluation of Tables 1 and 2 shows as expected that the use of the GAC term combined with the region one, provides a significant improvement compared to the conventional GAC term. This is due to the fact that the exclusive use of the edge detection techniques do not work on ultrasound images having contrast problems. The region term significantly improves the detection of edges and avoids local minima of energy. This kind of problem can be treated using other minimization alternatives other than a simple gradient descent, see e.g. [60,61].

As we can see, the use of LP+LML improves even more the already good results obtained by GAC+GML. Indeed, the change of intensity is one of the main problems encountered in the application of region-based methods on ultrasound images. On highly noisy images with local intensity variations, the region term can segment the blood part of the left ventricle as a single region. Certainly, the underlying assumption of a single tissue with Rayleigh statistics is not practical in such situations. The additional proposed term, based

on the phase information, is more robust to attenuation artifacts because it is theoretically invariant to the change of intensity.

The statistics in Table 1 and 2 suggest that segmentations by the LP+LML method are not as good as those obtained manually, but still close. This can be explained by what is seen in Fig. 3, where manual results are more regular, while automated results tend to have more details. Nevertheless, a large variance is noted. Our analysis on this behavior focuses mainly on the attenuation on some images that can be a factor influencing the variance. This reinforces our conclusion regarding the robustness of the proposed approach compared to other existing alternatives.

Looking at the simulated images results in Table 3, we can observe that although the measures are not very discriminative between the two models, but globally the local Gaussian model is less competitive in comparison to the local Rayleigh one. This observation is also demonstrated in Fig. 6.

The radius parameter r is very important for the segmentation process. It can be adjusted according to the image intensity inhomogeneities. It is advisable not to use a very small value of r to avoid a high variance in parameter estimation, nor a very large value to avoid a high bias. This parameter must be relatively small and sufficiently large. Using local statistics with an adaptive scale selection can be found in [13, 14, 15]. We also note that the localization adverse effect of FA discussed in the previous section can be corrected by the local region term.

7 Conclusion

A new model and a computational algorithm to segment B-mode ultrasound images has been presented. The technique is based on level-set methods and exploits the a priori knowledge about the statistical distribution of image gray levels. Ultrasound images characteristics, such as attenuation and low contrast, suggest the use of local image properties in order to improve robustness and accuracy. Conventional global region-based and intensity gradient-based methods have had limited success on typical clinical images. To avoid this drawback, local phase-based and local-statistics-based approaches offer a good alternative, since they make the approach robust to attenuation artifacts. It is within this framework that we propose an alternative in this paper. The quantitative and qualitative evaluations on natural and synthetic data show, as expected, that the use of phase-based edge detection with an additional local region term provides a significant improvement with respect to the classical ones of the same nature. The key advantage of this approach is that it is more robust to intensity inhomogeneities.

A Functional minimization

To compute the first variation of Equation (4), we express $F(\phi; \mathbf{x})$ as $F(\phi + \tau\psi; \mathbf{x})$ and take the partial derivative with respect to τ evaluated at $\tau = 0$. This allows us to represent a tiny differential of movement. Here, ψ represents a small perturbation along the normal direction of ϕ weighted by a scalar τ . In agreement to [54], we obtain

$$\left. \frac{\partial}{\partial \tau} F(\phi + \tau\psi; \mathbf{x}) \right|_{\tau=0} = \int_{\Omega} \delta(\phi(\mathbf{y})) \mathcal{B}(\mathbf{y}; \mathbf{x}) \times F_{LML}(\phi; \mathbf{y}; \mathbf{x}) \psi(\mathbf{y}) d\mathbf{y} \quad (8)$$

where $F_{LML}(\cdot)$ is the associated flow equation of $F(\cdot)$ as expressed in (6).

Starting from the local energy term $\mathcal{R}_L(\phi)$ given in (5), we get:

$$\mathcal{R}_L(\phi) = \int_{\Omega} \delta(\phi(\mathbf{x})) F(\phi; \mathbf{x}) d\mathbf{x} ,$$

the tiny differential of movement is given by

$$\left. \frac{\partial}{\partial \tau} \mathcal{R}_L(\phi + \tau \psi) \right|_{\tau=0} = \left. \frac{\partial}{\partial \tau} \left\{ \int_{\Omega} \delta(\phi(\mathbf{x}) + \tau \psi(\mathbf{x})) \times F(\phi + \tau \psi; \mathbf{x}) d\mathbf{x} \right\} \right|_{\tau=0} .$$

By the product rule, we obtain the following:

$$\begin{aligned} d\mathcal{R}_L(\phi, \psi) &= \int_{\Omega} \delta'(\phi(\mathbf{x})) \psi(\mathbf{x}) F(\phi; \mathbf{x}) d\mathbf{x} \\ &+ \int_{\Omega} \delta(\phi(\mathbf{x})) dF(\phi, \psi; \mathbf{x}) d\mathbf{x} , \end{aligned}$$

where $dF(\phi, \psi; \mathbf{x})$ denotes the directional derivative of $F(\phi; \mathbf{x})$ as presented in Equation (8). $\delta'(\phi)$ denotes the derivative of $\delta(\phi)$. This term is ignored, because it does not affect the movement of the curve [38]. The equation of $d\mathcal{R}_L(\phi, \psi)$ becomes:

$$\begin{aligned} d\mathcal{R}_L(\phi, \psi) &= \int_{\Omega} \delta(\phi(\mathbf{x})) \\ &\times \left\{ \int_{\Omega} \delta(\phi(\mathbf{y})) \mathcal{B}(\mathbf{y}; \mathbf{x}) F_{LML}(\phi; \mathbf{y}; \mathbf{x}) \psi(\mathbf{y}) d\mathbf{y} \right\} d\mathbf{x} . \end{aligned}$$

By moving the integral over \mathbf{y} outside the integral over \mathbf{x} we obtain:

$$\begin{aligned} d\mathcal{R}_L(\phi, \psi) &= \int_{\Omega} \int_{\Omega} \delta(\phi(\mathbf{x})) \delta(\phi(\mathbf{y})) \\ &\times \mathcal{B}(\mathbf{y}; \mathbf{x}) F_{LML}(\phi; \mathbf{y}; \mathbf{x}) \psi(\mathbf{y}) d\mathbf{x} d\mathbf{y} . \end{aligned}$$

From this equation it is easy to determine the associated flow:

$$\frac{\partial \phi}{\partial \tau}(\mathbf{x}) = \delta(\phi(\mathbf{x})) \int_{\Omega} \delta(\phi(\mathbf{y})) \mathcal{B}(\mathbf{y}; \mathbf{x}) F_{LML}(\phi; \mathbf{y}; \mathbf{x}) d\mathbf{y} .$$

Acknowledgements The authors would like to thank Rabeh Djabri for English proofreading and Dr. Mathiron and Dr. Levy for their help in the clinical evaluation. Part of this work was funded by the Regional Council of Picardie and European Union/FEDER.

References

1. Ahn, C. Y., Jung, Y. M., Kwon, O. I., Seo, J. K. : Fast segmentation of ultrasound images using robust Rayleigh distribution decomposition. *Pattern Recogn.* **45**(9), 3490–3500 (2012)
2. Alessandrini, M., Basarab, A., Liebgott, H., Bernard, O.: Myocardial Motion Estimation from Medical Images Using the Monogenic Signal. *IEEE Trans. Image Process.* **22**(3), 1084–1095 (2013).
3. Anquez, J., Angelini, E., Bloch, I.: Segmentation of fetal 3D ultrasound based on statistical prior and deformable model. In: *IEEE Int. Symp. Biomed. Imag.* pp. 17–20. Paris (2008)
4. Awate, SP, Tasdizen, T, Foster, N, Whitaker, RT: Adaptive Markov modeling for mutual-information-based, unsupervised MRI brain-tissue classification. *Med. Image Anal.* **10**(5), 726-739 (2006)
5. Aysal, T. C., Barner, K. E.: Rayleigh-maximum-likelihood filtering for speckle reduction of ultrasound images. *IEEE Trans. Med. Imag.* **26**(5), 712–27 (2007)
6. Belaid, A., Boukerroui, D., Maingourd, Y., Lerallut, J.F.: Implicit active contours for ultrasound images segmentation driven by phase information and local maximum likelihood. In: *IEEE Int. Symp. Biomed. Imag.* pp. 630–635. Chicago Illinois, USA (2011)

7. Belaid, A., Boukerroui, D., Maingourd, Y., Lerallut, J.F.: Phase based level set segmentation of ultrasound images. *IEEE Trans. Information Tech. Biomed.* **15**(1), 138–147 (2011)
8. Belaid, A., Boukerroui, D.: α scale spaces filters for phase based edge detection in ultrasound images. In: *IEEE Int. Symp. Biomed. Imag.*, pp. 1247–1250. Beijing, China (2014)
9. Belaid, A., Boukerroui, D.: A new generalised α scale spaces quadrature filters. *Pattern Recogn.* **47**(10), 3209–3224 (2014)
10. Bosch, J., Mitchell, S., Lelieveldt, B.P., Nijland, F., Kamp, O., Sonka, M., Reiber, J.H.: Automatic segmentation of echocardiographic sequences by active appearance motion models. *IEEE Trans. Med. Imaging* **21**(11), 1373–1383 (2002)
11. Boukerroui, D., Baskurt, A., Noble, J.A., Basset, O.: Segmentation of ultrasound images: multiresolution 2D and 3D algorithm based on global and local statistics. *Pattern Recogn. Lett.* **24**(4-5), 779–790 (2003)
12. Boukerroui, D., Noble, J.A., Brady, M.: On the choice of band-pass quadrature filters. *J. Math. Imag. Vision* **21**(1), 53–80 (2004)
13. Boukerroui, D.: A local rayleigh model with spatial scale selection for ultrasound image segmentation. In: *British Machine Vision Conference, (BMVC)*, Surrey, UK, Sep. 3-7, 1–12 (2012)
14. Boukerroui, D.: Optimal spatial scale for local region-based active contours. *Image Processing (ICIP), IEEE International Conference on*, 4393–4397 (2014)
15. Boukerroui, D.: Local statistical models for ultrasound image segmentation. *Biomedical Image Segmentation: Advances and Trends*, pp. 437 (2016)
16. Bovik, A.C.: On detecting edges in speckle imagery. *IEEE Trans. Acoust. Speech Signal Processing* **36**(10), 1618–1627 (1988)
17. Brox, T., Cremers, D.: On local region models and a statistical interpretation of the piecewise smooth Mumford-Shah functional. *Int. J. Comp. Vision* **84**(2), 184–193 (2009)
18. Brusseau, E., de Korte, C., Mastik, F., Schaar, J., van der Steen, A.: Fully automatic luminal contour segmentation in intracoronary ultrasound imaging—a statistical approach. *IEEE Trans. Med. Imag.* **23**(5), 554–566 (2004)
19. C. Chesnaud P. Refregier, V.B.: Statistical region snake-based segmentation adapted to different physical noise models. *IEEE Trans. Pattern Anal. Mach. Intell.* **21**(11), 1145–1157 (1999)
20. Caselles, V., Kimmel, R., Sapiro, G.: Geodesic active contours. *Int. J. Comp. Vision* **22**(1), 61–79 (1997)
21. Chalana, V., Linker, D.T., Haynor, D.R., Kim, Y.: A multiple active contour model for cardiac boundary detection on echocardiographic sequences. *IEEE Trans. Med. Imag.* **15**(3), 290–298 (1996)
22. Chalana, V., Linker, D.T., Haynor, D.R., Kim, Y.: A multiple active contour model for cardiac boundary detection on echocardiographic sequences. *IEEE Trans. Med. Imag.* **15**(3), 290–298 (1996)
23. Cootes, T.F., Taylor, C.J., Cooper, D.H., Graham, J.: Active shape models - their training and application. *Comput. Vis. Image Underst.* **61**(1), 38–59 (1995)
24. Cremers, D., Rousson, M., Deriche, R.: A review of statistical approaches to level set segmentation: Integrating color, texture, motion and shape. *Int. J. Comp. Vision* **72**(2), 195–215 (2007)
25. Deng, Y., Wang, Y., Shen, Y.: Speckle reduction of ultrasound images based on Rayleigh-trimmed anisotropic diffusion filter. *Pattern Recogn. Lett.* **32**(13), 1516–25 (2011)
26. Dietenbeck, T., Alessandrini, M., Barbosa, C., D’Hooge, J., Friboulet, D., Bernard, O.: Detection of the whole myocardium in 2D-echocardiography for multiple orientations using a geometrically constrained level-set. *Med. Image Anal.* **16**(2), 386–401 (2012).
27. Drukker, K., Giger M. L., V.M.A., Mendelson, E.B.: Computerized detection and classification of cancer on breast ultrasound. *Acad. Radiol.* **11**(5), 526–535 (2004)
28. Dutt, V., Greenleaf, J.F.: Ultrasound echo envelope analysis using a homodyned K distribution signal model. *Ultrason. Imag.* **16**(4), 265287 (1994)
29. Eltoft, T.: The rician inverse gaussian distribution: A new model for non-rayleigh signal amplitude statistics. *IEEE Trans. Image Process.* **14**(11), 1722–1735 (2005)
30. Felsberg, M., Sommer, G.: The monogenic signal. *IEEE Trans. Signal Process.* **49**(49), 3136–3144 (2001)
31. Felsberg, M., Sommer, G.: The monogenic scale-space: A unifying approach to phase-based image processing in scale-space. *J. Math. Imag. Vision* **21**(1), 5–26 (2004)
32. Fernandes, D., Sekine, M.: Suppression of Weibull radar clutter. *IEICE Trans. Comm.* E76-B, 1231–1235. (1993)
33. Heimann, T., Meinzer, H.P.: Statistical shape models for 3d medical image segmentation: A review. *Med. Image Anal.* **13**(4), 543–563 (2009)
34. Jacob, G., Noble, J., Behrenbruch, C., Kelion, A., Banning, A.: shape-space-based approach to tracking myocardial borders and quantifying regional left-ventricular function applied in echocardiography. *IEEE Trans. Med. Imag.* **21**(3), 226–238 (2002)
35. Jardim, S., Figueiredo, M.: Segmentation of fetal ultrasound images. *Ultrasound Med. Biol.* **31**(2), 243–250 (2005)

36. Jensen, J.: Field: A program for simulating ultrasound systems. In: 10th Nordic-Baltic Conf. on Biomedical Imag., vol. 34, pp. 351–353 (1996)
37. Kovese, P.: Image features from phase congruency. *Videre: J. Comput. Vis. Res.* **1**(3), 1–26 (1999)
38. Lankton, S., Tannenbaum, A.: Localizing region-based active contours. *IEEE Trans. Image Process.* **17**(11), 2029–2039 (2008)
39. Li, C., Kao, C., Gore, J., Ding, Z.: Implicit active contours driven by local binary fitting energy. In: Proc. of IEEE Conf. Comput. Vis. Pattern Recognit. (CVPR), pp. 1–7. IEEE Computer Society, Washington, DC, USA (2007)
40. Lin, N., Yu, W., Duncan, J.S.: Combinative multi-scale level set framework for echocardiographic image segmentation. *Med. Image Anal.* **7**, 529–537 (2003)
41. Martin-Fernandez, M., Alberola-Lopez, C.: An approach for contour detection of human kidneys from ultrasound images using markov random fields and active contours. *Med. Image Anal.* **9**(1), 21–23 (2005)
42. Mignotte, M., Collet, C., Prez, P., Bouthemy, P.: Three-class markovian segmentation of high-resolution sonar images. *CVIU* **76**(3), 191–204 (1999)
43. Morrone, M.C., Burr, D.C.: Feature detection in human vision: A phase-dependent energy model. In: Proc. R. Soc. Lond, B 235, pp. 221–245 (1988)
44. Mulet-Parada, M., Noble, J.A.: 2D+T acoustic boundary detection in echocardiography. In: MICCAI, pp. 806–813. Springer-Verlag, London, UK (1998)
45. Mulet-Parada, M., Noble, J.A.: 2D+T acoustic boundary detection in echocardiography. *Med. Image Anal.* **4**(1), 21 – 30 (2000)
46. Nadarajah, S.: Statistical distributions of potential interest in ultrasound speckle analysis. *Phys. Med. Biol.* **52**, 213–227 (2007)
47. Noble, J.A.: Ultrasound image segmentation and tissue characterization. *Proc. IMechE, Part H: J. Eng. Med.* **224**(2), 307–316 (2010)
48. Noble, J.A., Boukerroui, D.: Ultrasound image segmentation: A survey. *IEEE Trans. Med. Imag.* **25**(8), 987–1010 (2006)
49. Papadogiorgaki, M., Mezaris, V., Chatzizisis, Y.S., Giannoglou, G.D., Kompatsiaris, I.: Image analysis techniques for automated ivus contour detection. *Ultrasound Med. Biol.* **34**(9), 1482–1498 (2008)
50. Paragios, N., Jolly, M.P., Taron, M., Ramaraj, R.: Active shape models & segmentation of the left ventricle in echocardiography. In: Int. Conf. Scale Space Theories and PDEs methods in Computer Vision, ser. *Lect. Note Comput. Sci.*, vol. 3459, pp. 131–142 (2005)
51. Porras, A., Alessandrini, M., De Craene, M., Duchateau, N., Sitges, M., Bijnens, B., Delingette, H., Sermesant, M., D’Hooge, J., Frangi, A., Piella, G.: Improved Myocardial Motion Estimation Combining Tissue Doppler and B-Mode Echocardiographic Images. *IEEE Trans. Med. Imag.* **33**(11), 2098 – 2106 (2014).
52. Raju, B.L., Srinivasan, M.A.: Statistics of envelope of high-frequency ultrasonic backscatter from human skin in vivo. *IEEE Trans. Ultra. Fer. Freq. Control* **49**(6), 871882 (2002)
53. Roy, S., Carass, A., Bazin, P.L., Resnick, S., Prince, J.L.: Consistent segmentation using a Rician classifier. *Med. Image Anal.* **16**(6), 524535 (2012)
54. Sarti, A., Corsi, C., Mazzini, E., Lamberti, C.: Maximum likelihood segmentation of ultrasound images with rayleigh distribution. *IEEE Trans. Ultra. Fer. Freq. Control* **52**(6), 947–960 (2005)
55. Shankar, P.M.: A general statistical model for ultrasonic backscattering from tissues. *IEEE Trans. Ultra. Fer. Freq. Control* **47**(6), 727736 (2000).
56. Slabaugh, G., Unal, G., Wels, M., Fang, T., Rao, B.: Statistical region-based segmentation of ultrasound images. *Ultrasound Med. Biol.* **35**(5), 781–795 (2009)
57. Steen, E., Olstad, B.: Scale-space and boundary detection in ultrasonic imaging using nonlinear signal-adaptive anisotropic diffusion. In: Proc. SPIE Medical Imaging: Image processing (1994)
58. Song, Z., Awate, S.P., Licht, D.J., Gee J.C.: Clinical neonatal brain MRI segmentation using adaptive nonparametric data models and intensity-based Markov priors. In: Proc. Med. Image. Comput. Assist. Interv., 883-90 (2007)
59. Tagare, H.D., Madsen, E.L., Frank, G.R., Hobson, M.A.: Comprehensive evaluation of a cardiac ultrasound segmentation algorithm. *IEEE Trans. Med. Imag.* **25** (2007)
60. Tao, Z., Tagare, H.: Tunneling descent level set segmentation of ultrasound images. In: IPMI, pp. 750–761 (2005)
61. Tao, Z., Tagare, H.: Evaluation of four probability distribution models for speckle in clinical cardiac ultrasound images. *IEEE Trans. Med. Imag.* **25**(11), 1483–1491 (2006)
62. Tilmant, C., Sarry, L., Corpetti, T., Motrefi, P., Geoffroy, E., Lusson, J.R., Mmin, E., Boire, J.Y.: Suivi d’objets pour l’analyse du mouvement en imagerie ultrasonore. In: Congrès Jeunes Chercheurs en Vision par Ordinateur (ORASIS’05). Fournols, France (2005)

63. Tohka, J., Dinov, I.D., Shattuck, D.W., Toga, A.W.: Brain MRI tissue classification based on local Markov random fields. *Magn. Reson. Imaging* **28**(11), 557573 (2010)
64. Wang, L., He, L., Mishra, A., Li, C.: Active contours driven by local gaussian distribution fitting energy. *Signal Process.* **89**, 2435–2447 (2009)
65. Zaouche, R., Belaid, A., Aloui, S., Basel, S., Lecornu, L., Ben Salem, D., Tliba, S.: Semi-automatic method for low-grade gliomas segmentation in magnetic resonance imaging. *Innovation and Research in BioMedical Engineering*. Unpublished, (2018)
66. Zhang, W., Li, C., Noble, J.A., Brady, M.: Spatio-temporal segmentation of left ventricle in real-time 3D echocardiographic images using phase information. In: *Proc. Med. image Unders. and Anal. Aberystwyth* (2007)
67. Zhu, Y., Papademetris, X., Sinusas, A.J., Duncan, J.S.: A coupled deformable model for tracking myocardial borders from real-time echocardiography using an incompressibility constraint. *Med. Image Anal.* **14**(3) (2010)